

A merger-driven scenario for clumpy galaxy formation in the epoch of reionization: Physical properties of clumps in the FirstLight simulationYURINA NAKAZATO,¹ DANIEL CEVERINO,^{2,3} AND NAOKI YOSHIDA^{1,4,5}¹*Department of Physics, The University of Tokyo, 7-3-1 Hongo, Bunkyo, Tokyo 113-0033, Japan*²*Universidad Autonoma de Madrid, Ciudad Universitaria de Cantoblanco, E-28049 Madrid, Spain*³*CIAFF, Facultad de Ciencias, Universidad Autonoma de Madrid, E-28049 Madrid, Spain*⁴*Kavli Institute for the Physics and Mathematics of the Universe (WPI), UT Institute for Advanced Study, The University of Tokyo, Kashiwa, Chiba 277-8583, Japan*⁵*Research Center for the Early Universe, School of Science, The University of Tokyo, 7-3-1 Hongo, Bunkyo, Tokyo 113-0033, Japan***ABSTRACT**

Recent JWST observations with superb angular resolution have revealed the existence of clumpy galaxies at high redshift through the detection of rest-frame optical emission lines. We use the FirstLight simulation to study the properties of (sub-)galactic clumps that are bright in [OIII] 5007Å line with flux greater than $\sim 10^{-18} \text{ erg s}^{-1} \text{ cm}^{-2}$, to be detected by JWST. For 62 simulated galaxies that have stellar masses of $(0.5 - 6) \times 10^{10} M_{\odot}$ at $z = 5$, we find clumps in 1828 snapshots in the redshift range $z = 9.5 - 5.5$. The clumps are identified by the surface density of star formation rate. About one-tenth of the snapshots show the existence of clumpy systems with two or more components. Most of the clumps are formed by mergers and can be characterized by their ages; central clumps dominated by stellar populations older than 50 Myr, and off-centered clumps dominated by younger stellar populations with specific star formation rates of $\sim 50 \text{ Gyr}^{-1}$. The latter type of young clumps is formed from gas debris in the tidal tails of major mergers with baryonic mass ratios of $1 \leq q < 4$. The merger-induced clumps are short-lived, and merge within a dynamical time of several tens million years. The number density of the clumpy systems is estimated to be $\sim 10^{-5} \text{ cMpc}^{-3}$, which is large enough to be detected in recent JWST surveys.

1. INTRODUCTION

Recent observations by James Webb Space Telescope (JWST) have significantly advanced our understanding of galaxy formation and evolution in the early Universe. A number of high- z galaxies have been observed so far, and the record of the most distant galaxies has been renewed (e.g. Curtis-Lake et al. 2023; Wang et al. 2023; Arrabal Haro et al. 2023; Harikane et al. 2023a). For galaxies at $z \gtrsim 9.5$, strong rest-frame optical emission lines such as [OIII] 5007 Å are outside the range of JWST NIRSpec. Because of the vast distance, these galaxies appear typically as single-component systems and thus it is difficult to obtain detailed information on the kinematics and internal structure.

Galaxies at $z = 6 - 9$ are promising targets for detailed studies on clump formation and evolution using emission lines. NIRCам has a resolution of $0.03''$ /pixel

for long wavelength (2.4-5.0 μm), corresponding to $\sim 150 \text{ pc/pixel}$ at $z = 8$ ¹. NIRSpec Integral Field Unit (IFU) has a pixel scale of $0.05''$ ², corresponding to $\sim 250 \text{ pc/pixel}$ at $z = 8$. Gravitational lensing with magnification μ increases the effective spatial resolution by $\sqrt{\mu}$, allowing detailed studies of internal structure of galaxies (e.g. Hsiao et al. 2023a; Bradač et al. 2023; Álvarez-Márquez et al. 2023; Jones et al. 2023; Hashimoto et al. 2023). Hainline et al. (2023) studied over 700 galaxy candidates at $z > 8$ in JADES survey and found that a large number of them contain UV-bright star-forming clumps and/or elongated structures. A prominent example is JADES-GN-189.18051+62.18047 which consists of five clumps, and four of them are located within

¹ NIRCам has a pixel scale of $0.063''$ /pixel on the sky, but the post-process image data reduction allows the grid resolution $0.03''$ per pixel (Kashino et al. 2023; Matthee et al. 2023).

² NIRSpec IFU elements are $0.1''$ /pixel on the sky, but the combination of dithering and drizzle weighting allows sub-sampling of the detector pixels with $0.05''$ (Jones et al. 2023; Hashimoto et al. 2023).

a small region of ~ 7 kpc. Hashimoto et al. (2023) observed the central core region of a proto-cluster system at $z = 7.88$ using NIRSpec IFU, and the detection of [OIII] 5007 Å shows that four member galaxies are located in a ~ 11 kpc region. Jones et al. (2023) found a merging system of star-forming galaxies at $z \sim 6.3$, which consists of six galaxies within ~ 11 kpc. While these observations suggest rapid assembly of high redshift galaxies, it remains largely unknown how the compact clumpy systems emerge at the early epochs.

Numerical simulations have been utilized to follow clump formation within disk galaxies at lower redshift at $z = 0 - 4$ (e.g. Agertz et al. 2009; Ceverino et al. 2010; Mandelker et al. 2014, 2017; Buck et al. 2017; Ceverino et al. 2023). They have proposed two major mechanisms for clump formation: violent disk instability (VDI) and mergers. The former is driven by, for example, cold gas accretion flowing along the cosmic web (Dekel et al. 2009; Ceverino et al. 2010; Dekel & Krumholz 2013; Rodriguez-Gomez et al. 2016), and the local disk instability is often judged by Toomre parameter Q (Toomre 1964). Galaxy mergers cause significant gas density perturbations and even promote star formation (Di Matteo et al. 2008), and thus may be another promising formation path of clumps.

Both numerical simulations and observations suggest that the galaxy merger rate may increase at higher redshifts (e.g. Hopkins et al. 2010; Rodriguez-Gomez et al. 2015; Romano et al. 2021), and merger-driven clump formation may be relatively more important (Ribeiro et al. 2017) because the number of massive disks is generally smaller (Ceverino et al. 2015). Ribeiro et al. (2017) argue that the clump fraction increases from 35 to 50 percent from $z = 2$ to $z = 6$. Clumpy galaxies at $z = 5 - 7$ have been observed in rest-frame UV (e.g. Shibuya et al. 2016; Bowler et al. 2017; Shibuya et al. 2022; Bowler et al. 2022). The fraction of clumpy galaxies may also depend on stellar mass. Guo et al. (2015) present that $\sim 60\%$ of low-mass galaxies with $\log(M_*/M_\odot) < 9.8$ at $z = 0.5 - 3$ have clumpy structures.

Formation of clumpy galaxies at $z > 6$ is not well understood theoretically. There is a systematic difficulty with cosmological hydrodynamics simulations such as Illustris TNG (Pillepich et al. 2018) and Shimizu et al. (2014) which have a minimum resolution of a few hundred pc, making it hard to resolve internal structures of galaxies at high redshift. Zoom-in simulations can achieve better resolution but are often limited to only a few galaxy samples (Barrow et al. 2017; Ma et al. 2018; Katz et al. 2019; Arata et al. 2020; Gelli et al. 2020, 2021), making it difficult to study the statistical properties of clumpy galaxies.

In this paper, we use the FirstLight simulation suite, which achieves a very high resolution of 17 pc and provides a large sample size to allow robust statistical analysis. We use outputs for 62 simulated galaxies with 4092 snapshots in $z = 6 - 9$. Our main objective is to study the properties of galaxy clumps at the epoch of reionization, and their formation and evolution.

In our previous study (Nakazato et al. 2023), we devised a physical model of HII regions and calculated the luminosity of emission lines for the same FirstLight galaxy samples. The resulting relation between the star formation rate and [OIII] luminosity is consistent with recent observations (e.g. Hashimoto et al. 2018; Tamura et al. 2019; Harikane et al. 2020). We use the same model to characterize clumpy galaxies that are bright in rest-frame optical emission lines such as [OIII] 5007 Å.

The rest of the present paper is organized as follows. In Section 2, we introduce the numerical simulation and describe the method to calculate line luminosities and to define clumps. In Section 3, we discuss in detail the formation and evolution of a few clumpy systems. Summary and conclusions are given in Section 4. Throughout this paper, we assume a set of parameters in Λ CDM cosmology with $\Omega_m = 0.307$, $\Omega_b = 0.048$, $h = 0.678$ and $\sigma_8 = 0.823$ from *Planck13* results (Planck Collaboration et al. 2014).

2. METHOD

2.1. Zoom-in Simulation

We use the cosmological zoom-in simulation suite FirstLight (Ceverino et al. 2017). The simulations are performed using the ART code (Kravtsov et al. 1997; Kravtsov 2003), which follows gravitational N -body dynamics and Eulerian hydrodynamics with Adaptive Mesh Refinement (AMR). The parent simulation has a box size of 40 comoving h^{-1} Mpc on a side. We identified the 62 most massive halos in the parent dark matter only simulation. The halos have maximum rotation velocities with $V_{\max} > 178 \text{ km s}^{-1}$ at $z = 5$. We then performed zoom-in simulations in these regions with an effective resolution of 4096^3 and a maximum resolution of 17-32 proper pc. The dark matter particle mass is $8 \times 10^4 M_\odot$ and the minimum stellar particle mass is $10^3 M_\odot$. The zoom-in simulations follow radiative cooling by atomic hydrogen and helium, metal ions and atoms, and molecular hydrogen, and photoionization heating by a time-dependent UV background with partial self-shielding. A number of baryonic processes in star formation and feedback are incorporated in a sub-grid manner. More details are described in Ceverino & Klypin (2009) and Ceverino et al. (2014, 2017). The FirstLight galaxies have stellar masses greater than $\sim 10^{10} M_\odot$ at $z = 5$.

We store a total of 66 snapshots between $z = 9.5$ to $z = 5.5$ for each galaxy, with a spacing of the cosmic expansion parameter $\Delta a = 0.001$, corresponding to 7 – 10 Myr³. The frequent output timing is sufficient to follow dynamics during galaxy mergers that occur on the tidal timescale of 10-100 Myrs (Renaud et al. 2013).

2.2. Line luminosity Calculation

We calculate the luminosities of emission lines from HII regions for the simulated galaxies and clumps. We adopt essentially the same model as Nakazato et al. (2023) and assume that each stellar particle is surrounded by a spherical HII region. We generate a table of a set of emission lines using CLOUDY (Ferland et al. 2013). The input stellar SEDs are calculated using Binary Population and Spectral Synthesis (BPASS) model (Eldridge et al. 2017). The input parameters for CLOUDY are gas metallicity Z_{gas} , ionization parameter U , and gas density in HII regions n_{HII} . The adopted values of the parameters are listed in Table 1. In our table, we normalize the emission line luminosity for each stellar particle ($L_{\text{line},i}$) by $\text{H}\beta$ luminosity as

$$L_{\text{line},i} = (1 - f_{\text{esc}}) C_{\text{line}}(Z_{\text{gas}}, U, n_{\text{HII}}) L_{\text{H}\beta}^{\text{caseB}}. \quad (1)$$

Here f_{esc} is the escape fraction and we assume $f_{\text{esc}} = 0.1$. Our model assumes that the gas density of a HII region is given by

$$n_{\text{HII}} = \begin{cases} 100 \text{ cm}^{-3} & (n_{\text{gas,grid}} < 100 \text{ cm}^{-3}) \\ n_{\text{gas,grid}} & (n_{\text{gas,grid}} \geq 100 \text{ cm}^{-3}), \end{cases} \quad (2)$$

where $n_{\text{gas,grid}}$ is the gas number density of a grid with a size of $\Delta = 50 \text{ pc}$. The threshold value is determined by the typical density of HII regions (Osterbrock & Ferland 2006; Hirschmann et al. 2017, 2022). The variable n_{HII} is motivated by recent JWST observations that imply an apparent redshift evolution of n_{HII} (Isobe et al. 2023; Fujimoto et al. 2022)⁴. We look for the line ratio table C_{line} with the three parameters Z_{gas} , U , n_{HII} which are closest to those of the target stellar particles in our simulation. We obtain the line luminosity for each grid as $L_{\text{line,grid}} = \sum_i^N L_{\text{line},i}$, where N is the number of stellar particles that the grid contains.

³ The time step width in the simulation is much shorter than this, being typically 1000 years.

⁴ Nakazato et al. (2023) assumed the fixed HII density as $n_{\text{HII}} = 100 \text{ cm}^{-3}$. We also have checked the dependency of $[\text{OIII}]$ 5007 Å luminosity on the density model and found that the value changes within only $\lesssim 1 \%$.

$\log_{10} (Z_{\text{gas}}/Z_{\odot})$	-1.30, -0.70, -0.40, 0., 0.30
$\log_{10} U$	-4.0, -3.9, ..., -1.1, -1.0
$\log_{10} (n_{\text{HII}}/\text{cm}^{-3})$	1.0, 2.0, 3.0

Table 1. The parameters used to calculate the line luminosities with CLOUDY.

In our previous study (Nakazato et al. 2023; Mushtaq et al. 2023), we find that the magnitude of dust attenuation at rest-frame 5007 Å is approximately $A_{5007} = 0.08, 0.24, 0.7$ for individual *galaxies* with $M_*/M_{\odot} = 10^8, 10^9, 10^{10}$, respectively. Thus, we expect that dust attenuation affects the line luminosity of a small clump by a factor of a few. We further discuss this issue of dust attenuation in Section 4.

2.3. Clump Finder

In order to compare the properties of the simulated clumpy galaxies with observations, we identify clumps in two-dimensional “images”, using projection along a random line of sight (z -axis) of a cube with a fixed side length of 10 kpc. The size is larger than the main central galaxy, and is close to a field of view of NIRSpec IFU at $z = 8$. We assign masses of gas, stars and dark matter to a uniform grid with $\Delta = 50 \text{ pc}$ by using a cloud-in-cell interpolation also employed in Mandelker et al. (2014, 2017) and Ceverino et al. (2023). We first mark grids that contain young ($< 10 \text{ Myr}$) stars with their surface mass density greater than $10^{8.5} M_{\odot}/\text{kpc}^2$, and then identify candidate groups by running a Friends-of-Friends finder with linking length Δ to the marked grids. Groups with at least 16 grids are identified as clumps. The threshold surface stellar mass density and the minimum number of grids are chosen to ensure that the identified clumps are resolved by observations by NIRSpec IFU ($\sim 250 \text{ pc}$) and NIRCам WFSS ($\sim 150 \text{ pc}$) with the line flux of $F_{[\text{OIII}]} \gtrsim 10^{-18} \text{ erg s}^{-1} \text{ cm}^{-2}$ at $z = 8$. We have also checked the effect of line of sight by changing inclination and it does not change the number of clumps.

2.3.1. Parameter determination

We set three parameters for our clump finder; grid size (Δ), threshold surface mass density of young stellar population ($\Sigma_{M_*(\text{young})}$), and the minimum number of grids (N_{grid}). The grid size is set to be larger than the Strömgren radius for each stellar particle in our line emission model. We assume that a HII region exists around each stellar particle. The Strömgren radius R_s

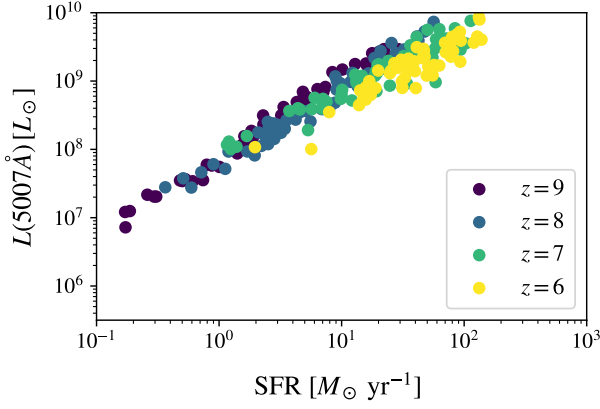


Figure 1. The [OIII] 5007 Å luminosity vs. SFR for our 62 simulated galaxies at $z = 9$ (purple), 8 (blue), 7 (green), and 6 (yellow).

is given by

$$R_s = \left(\frac{3Q_0}{4\pi n_{\text{HII}}^2 \alpha_B} \right)^{1/3} \quad (3)$$

$$= 5.4 \text{ pc} \left(\frac{n_{\text{HII}}}{10^2 \text{ cm}^{-3}} \right)^{-2/3} \left(\frac{Q_0}{5 \times 10^{49} \text{ s}^{-1}} \right)^{1/3}, \quad (4)$$

where n_{HII} is the gas density in HII regions and Q_0 is the number of ionizing photons per unit time. The electron temperature is $T_e = 10^4 \text{ K}$ and a filling factor of $\epsilon = 1$ is assumed. The median (maximum) value of Q_0 is 5×10^{50} (5×10^{52}) s^{-1} for all the particles in the simulation, and the corresponding Strömgren radius is $R_s \sim 15$ (54) pc for $n_{\text{HII}} = 100 \text{ cm}^{-3}$. We thus set $\Delta = 50 \text{ pc}$, which is 2-4 times the maximal AMR resolution.

To determine the threshold of projected stellar mass, we consider the relationship between $L_{[\text{OIII}] 5007\text{Å}}$ and star formation rate (SFR). Figure 1 shows the [OIII] 5007 Å luminosity against SFR for our galaxy samples. It is approximated as⁵

$$L_{[\text{OIII}] 5007\text{Å}} \sim 6 \times 10^7 \left(\frac{\text{SFR}}{M_\odot \text{ yr}^{-1}} \right) L_\odot \quad (5)$$

$$\sim 6 \times \left(\frac{M_{*,(\text{young})}}{M_\odot} \right) L_\odot, \quad (6)$$

⁵ Our linear fitted line for each redshift is

$$\log_{10} L_{[\text{OIII}]} [L_\odot] = 1.16 \times \log_{10} \text{SFR} + 7.89 \quad (z = 9)$$

$$\log_{10} L_{[\text{OIII}]} [L_\odot] = 1.16 \times \log_{10} \text{SFR} + 7.74 \quad (z = 8)$$

$$\log_{10} L_{[\text{OIII}]} [L_\odot] = 0.87 \times \log_{10} \text{SFR} + 7.97 \quad (z = 7)$$

$$\log_{10} L_{[\text{OIII}]} [L_\odot] = 0.97 \times \log_{10} \text{SFR} + 7.67 \quad (z = 6).$$

where $M_{*,(\text{young})}$ is the mass of very young (< 10 Myrs) stars and the instantaneous SFR is estimated as $(M_{*,(\text{young})}/10^7) M_\odot \text{ yr}^{-1}$. The flux limit to detect a clump by [OIII] 5007 Å line is $\sim 3 \times 10^{-18} \text{ erg s}^{-1} \text{ cm}^{-2}$, which corresponds to signal-to-noise ratio of $S/N > 5$ with an exposure time of $\sim 10^4 \text{ sec}$ (Hashimoto et al. 2018; Jones et al. 2023; Arribas et al. 2023; Matthee et al. 2023). The corresponding luminosity is $L_{[\text{OIII}] 5007\text{Å}} \sim 6 \times 10^7 L_\odot$ at $z = 8$. Substituting this into eq.(6), we obtain $M_{*,(\text{young})} \sim 10^7 M_\odot$ for a “detectable” clump. For the threshold grid number, we set $N_{\text{grid}} = 16$. This translates to a minimum clump radius of $\sim 100 \text{ pc}$, which is one dex larger than the minimum AMR resolution of 17 pc and can be resolved by recent JWST NIRCам/NIRSpec IFU observations. We have also checked other clump candidates with less than 16 grids. Most of them consist of one or two grids and they are too faint to be observed as clumps. If a clump consists of $N_{\text{grid}} = 16$ grids, each grid should have a surface stellar mass density of $\Sigma_{M_{*,(\text{young})}} \geq 10^6 M_\odot/\text{grid} = 10^{8.5} M_\odot/\text{kpc}^2$, where one grid area is $\Delta^2 = 50^2 \text{ pc}^2$. This value is the threshold we use to identify clumps.

3. RESULT

3.1. Projection of physical properties for simulated clumpy galaxies

Figure 2 shows three examples of simulated galaxies. Two, four, and three clumps are identified in these outputs as bright components. The clumps trace the distribution of young stars but also that of dense gas with $n_{\text{gas}} \gtrsim 100 \text{ cm}^{-3}$. Tail features can be also seen in [OIII] emission, similar to recent several galaxies observed by JWST such as MACS1149-JD1 ($z = 9.1$, Bradač et al. 2023) and B14-65666 ($z = 7.15$, Sugahara et al. in prep.). The distribution of the stars older than 100 Myrs appears more diffuse than the young stellar population. The underlying dark matter distribution shows signatures of mergers, which will be explained in detail in Section 3.3. Some clumps (e.g. clump C in Figure 2) are located off-center. The clumps are separated with $\sim 0.1 - 4 \text{ kpc}$ distances, similarly to the clumps at $z \simeq 6 - 8$ studied by Chen et al. (2023), with typical separations of $\sim 0.3 - 4.3 \text{ kpc}$. Such close clumps are also found in other JWST observations at $z > 6$; JADES (Hainline et al. 2023), EIGER (Matthee et al. 2023) and CANUCS (Asada et al. 2024) surveys. The stellar age distributions in the right-most panels show a clear difference in the distribution of young and old components. Interestingly, similar features are found by JWST MIRI observations (e.g. Colina et al. 2023).

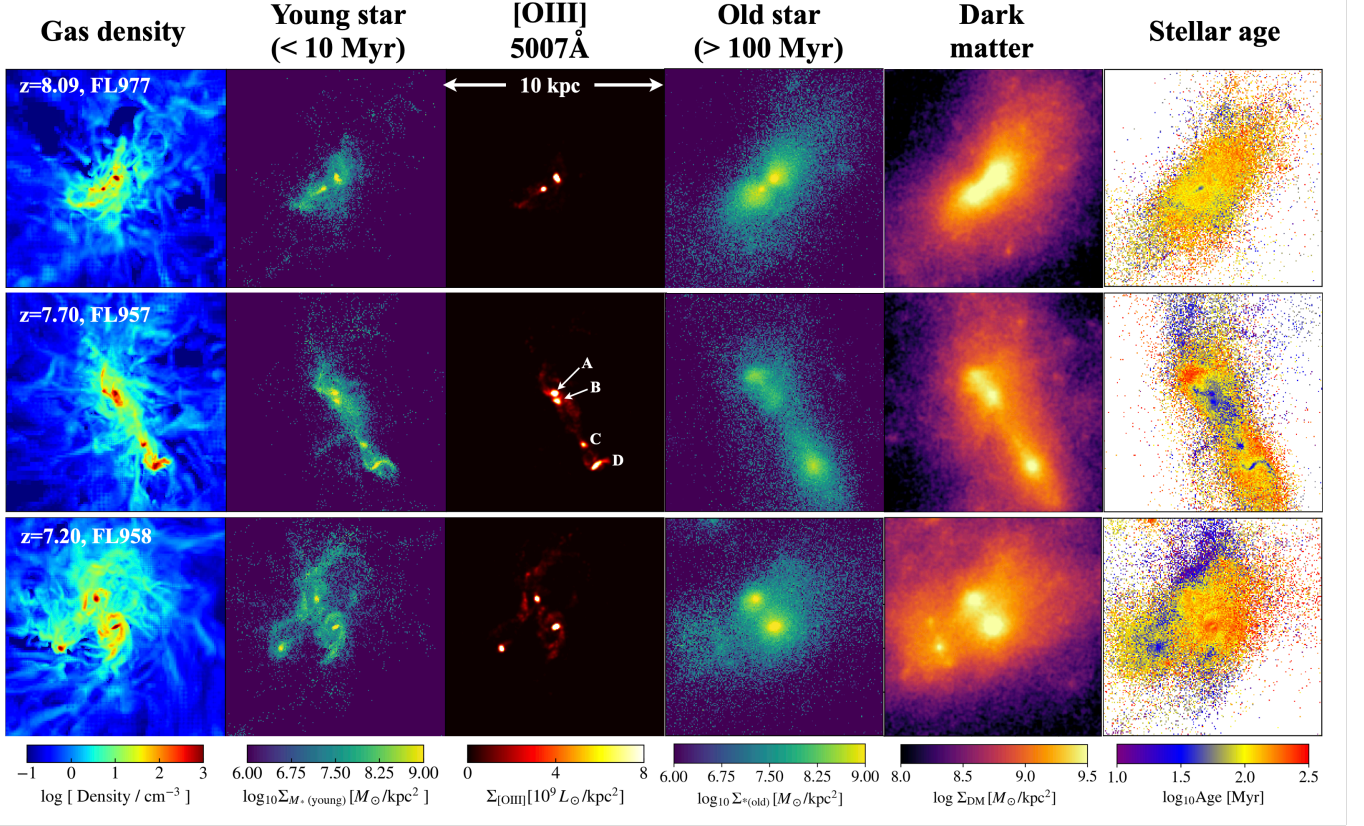


Figure 2. Three simulated clumpy galaxies at $z = 9.00$ (top, ID=FL977), $z = 7.70$ (middle, ID=FL957), and $z = 7.20$ (bottom, ID=FL958). Each column from left to right represents the averaged gas density, surface stellar mass density of young (< 10 Myr) population, [OIII] 5007 Å line flux, surface mass density of old (> 100 Myr) stellar population and dark matter, and mass-weighted stellar age, respectively. Each panel has a side length of 10 proper kpc and the same size of projected depth.

The panels in the middle row focus on the galaxy FL957, which contains the highest number of clumps at $z > 6$. To see if those clumps are gravitationally bounded or not, we have estimated the virial parameter (Bertoldi & McKee 1992), $\alpha_{\text{vir}} \equiv 5\sigma_{\text{clump}}^2 R_c / GM$, where σ_{clump} and R_c are velocity dispersion within a clump and clump radius. All clumps have $\alpha \sim 0.2$, which indicates that these clumps are gravitationally bound.

The four-clump feature motivates us to compare it with the recent observation by Hashimoto et al. (2023), who spectroscopically studied the core of the most distant protocluster at $z = 7.88$, A2744-z7p9OD, with JWST NIRSpec integral field spectroscopy. The core region contains four clumps which are detected by [OIII] 5007 Å in a region of $\sim 11 \times 11$ kpc. Table 2 summarizes the clump properties. We find that the stellar mass, SFR, and [OIII] luminosities are similar to the observed clumps (see Table 1 in Hashimoto et al. (2023)). These clump properties are typical for clumps younger than 50 Myrs identified in the clumpy systems as shown in Table 3, which is discussed in the next section. We discuss that such properties are different from clumps

older than 50 Myr in Section 3.2. In Sections 3.3 and 3.4, we show the formation and evolution of multi-clump systems.

3.2. Distributions of clump properties

Our clump finder identifies 2254 clumps in total. Of these, 1503 clumps are single systems, i.e. galaxies with one clump, often appearing as proto-bulge components. The remaining 751 clumps are in 325 clumpy systems. Table 3 summarizes the physical properties of the clumps. Figure 3 shows the distribution of the clump age weighted by stellar mass for single and multi-clump objects. The distribution for single systems has a peak at ~ 200 Myr, while the clumps in clumpy systems have a peak at ~ 90 Myr. Based on the age distribution, we can separate into two types of clumps: clumps younger than 50 Myr and clumps older than 50 Myr, which are indicated by blue and red histograms, respectively. Table 3 also shows the properties of clumps younger than 50 Myr and older than 50 Myr, respectively. We see that old clumps have similar stellar mass, age, and clump size to the clumps identified in single systems. Young clumps are smaller and their stellar mass

	$M_{*,(\text{young})} [M_{\odot}]$	$M_{*,(\text{all})} [M_{\odot}]$	SFR [M_{\odot}/yr]	$L_{[\text{OIII}]\,5007\text{\AA}} [L_{\odot}]$	$R_c [\text{pc}]$	Age [Myr]
A	8.32×10^7	1.32×10^8	8.32	1.10×10^9	157	39
B	4.62×10^7	1.87×10^8	4.62	5.59×10^8	138	27
C	2.45×10^7	3.76×10^7	2.45	2.85×10^8	116	34
D	8.49×10^7	3.32×10^8	8.49	9.14×10^8	155	30

Table 2. Summary of properties of FL957 at $z = 7.70$, which contains four clumps within 10×10 kpc region. Note that $M_{*,(\text{young})}$ refers to stellar masses younger than 10 Myrs and $M_{*,(\text{all})}$ are stellar masses for all ages. A clump radius R_c in the 5th column is obtained as $R_c = \sqrt{\Delta^2 N_{\text{grid}}/\pi}$.

	# of clumps	$M_{*,(\text{all})} [M_{\odot}]$	$n_{\text{gas,clump}} [\text{cm}^{-3}]$	Age [Myr]	$R_c [\text{pc}]$
single system	1503	5.2×10^9	283	134	234
clumpy system (total)	751	2.5×10^9	241	108	180
clumpy system (< 50 Myr)	182	2.7×10^8	269	35	142
clumpy system (> 50 Myr)	569	3.2×10^9	232	131	192
(single + clumpy) system	2254	4.3×10^9	269	125	216

Table 3. Summary of physical properties of galaxies we identify in single systems and clumpy systems. The clumps in clumpy systems are further categorized into two groups: those with ages younger than 50 Myr and older than 50 Myr. The last row of the table lists the average values for both systems. We see that old clumps (> 50 Myr) in clumpy systems have similar properties to ones in single systems as discussed in section 3.2.

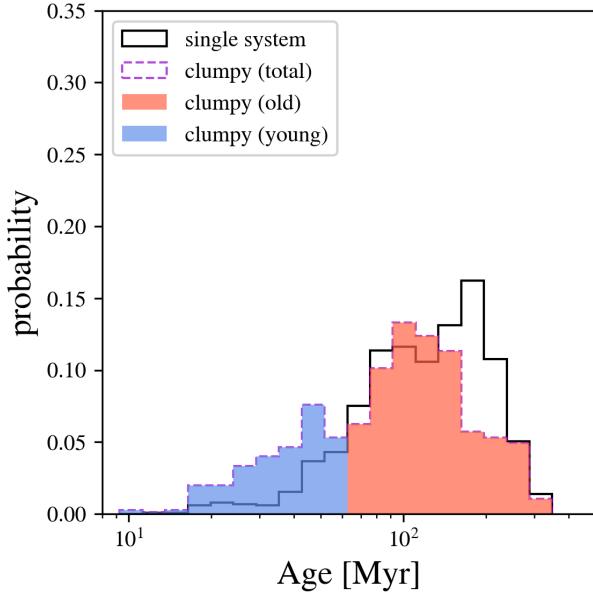


Figure 3. The distribution of mass-weighted clump ages. Black and dashed-purple histograms represent single systems (detected one central clump, i.e. proto-bulge) and clumpy systems, respectively. The histograms are normalized by the total number of clumps for each system. We divide the clumpy system into clumps younger than 50 Myrs (blue) and those older than 50 Myrs (red).

is 10 times lower than older clumps. Figure 4 shows the distributions of three properties for different systems: single systems with one clump ($N_{\text{clump}} = 1$, black solid line), and young and old clumps in clumpy systems

($N_{\text{clump}} \geq 2$, red and blue). The probability distributions are normalized to the total number of clumps in each of the three systems.

The left panel of Figure 4 refers to the gas fraction ($f_{\text{gas}} \equiv M_{\text{gas}}/M_{\text{baryon}}$) of individual clumps. Single systems have a distribution in the range of $f_{\text{gas}} \sim 0.4 - 0.95$ and have the peak at roughly $f_{\text{gas}} \sim 0.85$. While clumps younger than 50 Myrs concentrate on the value of 0.95, clumps older than 50 Myrs have almost the same distribution as single systems.

The middle panel of Figure 4 refers to the surface mass ratio of baryon and dark matter. Single systems have a peak at $\Sigma_{\text{baryon}}/\Sigma_{\text{DM}} \sim 10$, and the clumps older than 50 Myr have almost the same distribution and peak value. The shape of the distribution of clumps younger than 50 Myr is similar to the old ones, but the peak is shifted to a 0.5 dex larger value. This implies that over 50% of young clumps are formed off-center of their host dark matter halos, in a baryonic-rich environment.

The right panel of Figure 4 refers to the sSFR of individual clumps. The peak of the distribution for single systems is at $\text{sSFR} \sim 6 \text{ Gyr}^{-1}$, while the peaks for old and young clumps are at ~ 10 and 55 Gyr^{-1} , respectively. The sSFR values of single systems and old ($> 50 \text{ Myr}$) clumps in clumpy systems are similar to that of main-sequence galaxies at $z \sim 6$, $\text{sSFR} \sim 6 \text{ Gyr}^{-1}$ (Popesso et al. 2023). However, young clumps in clumpy systems have over 9 times larger sSFR than that of main-sequence galaxies, and such large values are also seen in observed merging galaxies at $z > 6$ (e.g. Sugahara et al. in prep.).

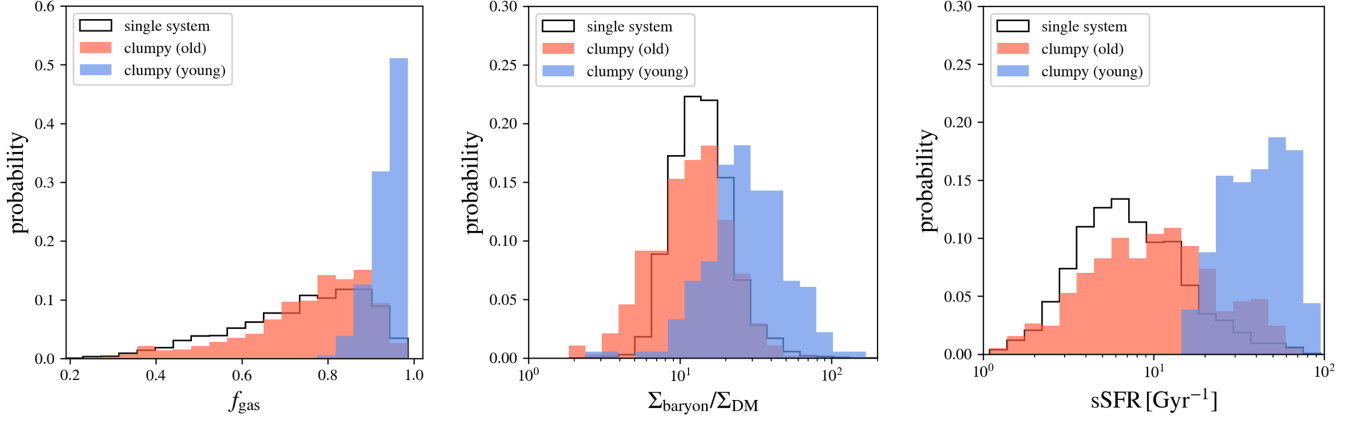


Figure 4. The probability distribution of the gas fraction, baryon-to-dark matter mass ratio, and specific star formation rate for our clump samples. The histograms with black solid lines are for single systems, We color the histograms for clumps depending on their age. The distributions are normalized to the total number of clumps in each of the colored types.

From the three physical properties in Figure 4, we see that clumps older than 50 Myr tend to have the same properties as single systems. On the other hand, clumps younger than 50 Myr are located in baryonic-rich environments. They are also gas-rich and in the process of bursty star formation. This indicates a different formation path for young clumps.

3.3. Clump formation induced by merger

In this section, we study the formation of clumps during a merger. The top panels of Figure 5 show the time evolution of dark matter distribution around FL957, and the bottom panels represent gas density distribution in the same central region of 10 kpc. At $z = 8.01$, we see two dark matter halos, one in the center of the panel and the other one in the right bottom. The two galaxies experience the first pericenter passage at $z = 7.85$, which enhances the tidal compression of the surrounding gas and forms dense clumps. After the first passage ($z = 7.70$), we identify four clumps and this number is larger than that of merging halos. These clumps are formed off-center from the halos. Tail structures coming from clumps are formed by tidal effects during the galaxy interaction⁶. The formation of star clusters triggered by galaxy merger has been already investigated by non-cosmological Antennae-like simulations (e.g. Renaud et al. 2013, 2014, 2015). These previous studies have found that the first two pericenter passages increase compressive (curl-free) turbulence and lead to clumpy morphologies and bursty star formation with the timescale of 10-30 Myr, whose results are consistent with

our results obtained from cosmological simulations at high redshift.

We estimate the mass of a perturber that generates clumps as follows. A merger-induced clump is formed if the mass is

$$M_{\text{clump}} = \bar{\rho}\delta \times V_{\text{clump}} \gtrsim M_{\text{min}}, \quad (7)$$

where M_{min} is the minimum baryon mass of the observable clump we define. Here, $\bar{\rho}$, δ , V_{clump} are the mean gas density around the progenitor, typical overdensity induced by the merger, and volume of the formed clump. Assuming that the perturber compresses the surrounding gas contained in a volume with its size $\sim R_{\text{per}}$, the formed clump mass is re-written as

$$M_{\text{clump}} = 2 \times 10^8 M_{\odot} \left(\frac{\bar{\rho}\delta}{250 \text{ cm}^{-3}} \right) \left(\frac{R_{\text{per}}}{200 \text{ pc}} \right)^3. \quad (8)$$

We normalize the relevant quantities by typical values found in our simulations (Table 3). For example, $\bar{\rho}\delta \sim 250 \text{ cm}^{-3}$. The minimum mass of a clump that emits [OIII] line bright enough to be observed is derived based on the young stellar mass criteria $M_{*(\text{young}),\text{min}} = 10^7 M_{\odot}$ in section 2.3.1,

$$M_{\text{min}} \sim \frac{M_{*(\text{young}),\text{min}}}{1 - f_{\text{gas}}} = 10^8 M_{\odot} \left(\frac{1 - f_{\text{gas}}}{0.1} \right)^{-1}, \quad (9)$$

where f_{gas} is the gas fraction defined in section 3.2. Young clumps have $f_{\text{gas}} \sim 0.9$ (Figure 4). Substituting equations (8) and (9) into eq.(7), we obtain the characteristic size of the baryonic “wake” induced by merger encounter (perturber) as $R_{\text{per}} \gtrsim 150 - 200 \text{ pc}$. The mass ratio $q \equiv M_{\text{center}}/M_{\text{per}}$ largely determines the subsequent morphological evolution and the mode of triggered star formation. We assume the central one

⁶ The movie of clump formation is obtained [here](#).

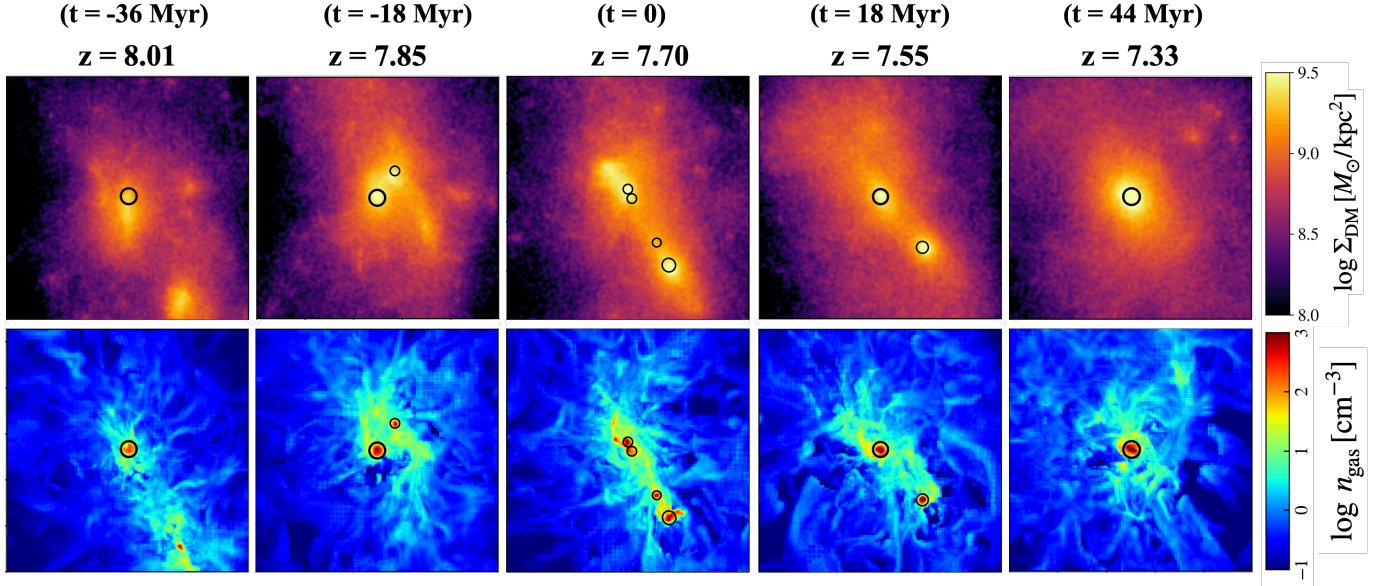


Figure 5. Time evolution of dark matter density (top) and gas density distribution (bottom) from $z = 8.01$ to $z = 7.33$. The side and projected lengths are 10 kpc for both projections. The black circles represent the location of the identified clumps. We set $t = 0$ at $z = 7.70$, when the galaxy consists of four luminous clumps.

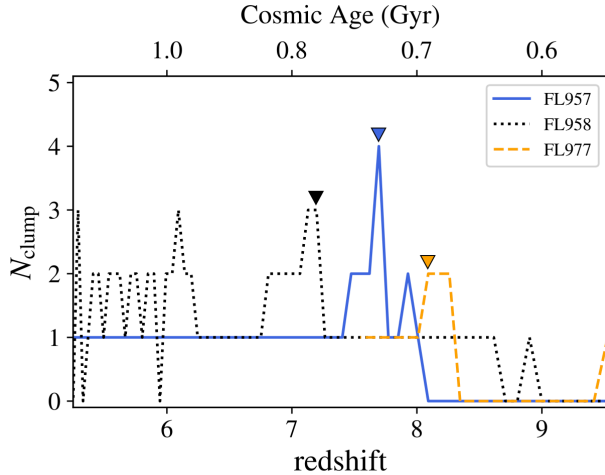


Figure 6. Time evolution of clump number as a function of redshift for the three galaxies shown in Figure 2. The inverted triangles represent the redshifts in Figure 2. $N_{\text{clump}} = 0$ represents that clumps are too faint to be identified by the clump finder.

is more massive, i.e., $M_{\text{center}} \geq M_{\text{per}}$. Considering that the central object in the system has a typical size of $R_{\text{center}} \simeq 200 - 230$ pc as listed in Table 3 and assuming that both objects have similar gas densities, we estimate the mass ratio to be $q = (R_{\text{center}}/R_{\text{per}})^3 = 1 - 3.6$. We thus argue that bright clumpy galaxies in optical emission lines at $z > 6$ can be formed by a major merger.

3.4. Clump fate

Figure 5 also follows the subsequent evolution of the clumpy system. A further 18 Myr after the formation of the four clumps. Clump B and C merge with clump A and D resulting in two clumps, which finally merge into a single system 26 Myrs later. Figure 6 shows the redshift evolution of the number of clumps for the three galaxies shown in Figure 2. Clumpy structures are observed temporarily and finally merge into the center of the system 30-40 Myr after the multiple systems are formed, whose evolution is seen in other galaxy samples. The typical timescale is the crossing time during the merger:

$$t_{\text{cross}} = \frac{d}{v - v_{\text{center}}} \sim 50 \text{ Myr} \left(\frac{d}{3 \text{ kpc}} \right) \left(\frac{v - v_{\text{center}}}{60 \text{ km/s}} \right)^{-1}, \quad (10)$$

where d and v_{center} are the separation and the velocity of the central object. The derived crossing timescale is consistent with the merger timescale in Figure 5, and roughly the same order of the orbital (dynamical) timescale of this system in a 10 kpc region, $t_{\text{orb}} \sim t_{\text{dyn}} \sim 25$ Myr. Therefore, we see that clumpy systems which are bright in rest-frame optical emission lines are temporary structures and finally merge into one massive galaxy within ~ 50 Myr.

Notice that the two galaxy systems (FL957, FL977) in Figure 6 are identified as $N_{\text{clump}} = 0$ at $z \sim 9$. This implies that these galaxies are too faint to be identified as an [OIII] bright object at $z \sim 9$. As noted in Section 2, our clump identification is based on surface SFR density. However, a lensing effect enables us to identify clumpy

features even at $z \gtrsim 9$ as the recent observations report triply lensed galaxies at $z = 10.17$ (Hsiao et al. 2023a,b).

3.5. number abundance of clumpy galaxies

Figure 7 represents the fraction of clump number at each redshift. Around 90% of galaxies at $z = 8 - 6$ are observed as a single system ($N_{\text{clump}} = 1$). From Table 2 and 3, we see that both observable clumpy galaxies tend to have stellar masses of $M_* \gtrsim 10^9 M_\odot$ in their systems, even though our clump definition sets a minimum clump mass of $M_* \geq M_{*(\text{young}),\text{min}} = 10^7 M_\odot$. Our sample galaxies at $z \geq 8.5$ have small stellar masses of $M_* \lesssim 10^9 M_\odot$, resulting in that all of our samples at $8.5 \leq z \leq 9$ are identified as a single system. At these high-redshifts, the corresponding UV magnitude of $M_{\text{UV}} \gtrsim -19.7$ ⁷. Galaxies at $z \lesssim 8$ are bright ($M_{\text{UV}} < -19.7$) and multiple clumps are identified, which are formed by mergers. This trend is interestingly consistent with the recent JWST observations of Chen et al. (2023), who find that luminous $z \simeq 6 - 8$ galaxies with $M_{\text{UV}} < -20.7$ tend to have 3-4 clumps and fainter galaxies with $M_{\text{UV}} > -20.7$ tend to be a single system. The fraction of galaxies with three more clumps ($N_{\text{clump}} \geq 3$) is $\sim 0.5 - 1\%$.

We do not find any clumpy systems formed by violent disk instability (VDI) through cold accretion until $z \sim 6$. This is because VDI requires a massive disk with a large disk mass fraction (Dekel et al. 2009; Ceverino et al. 2010). We identify some disk-like galaxies at $z = 8 - 9$, but the stellar masses are $\lesssim 5 \times 10^9 M_\odot$ and have smoothed disk. Specifically, two galaxies with five clumps are seen in a massive system, the total stellar mass in the field is $M_* \sim 10^{10} M_\odot$ at $z \sim 5.5$. The clumps in such a massive system are expected to be formed via violent disk instability as same as lower-redshift galaxies (Mandelker et al. 2014, 2017; Ceverino et al. 2023).

Figure 8 shows the number density of clumpy galaxies. As described in Section 2.1, our study employs zoom-in simulations and we need to correct for incompleteness in the number count of clumpy galaxies. We use the results of a larger boxsize N -body simulation (Klypin et al. 2011) (refer to Appendix A for details). The number density of single systems is $(1 - 3) \times 10^{-4} \text{ cMpc}^{-3}$

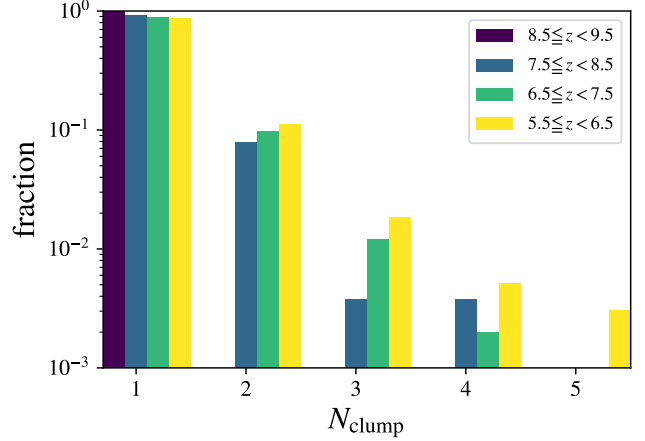


Figure 7. The fraction of each clump number at $z \sim 9$ (purple), $z \sim 8$ (blue), $z \sim 7$ (green), and $z \sim 6$ (yellow). The clump number N_{clump} is referred to as the number of clumps in the galaxy system within $10 \text{ kpc} \times 10 \text{ kpc}$ region.

at $z = 6 - 9$. We identify all the simulated galaxies at $z = 9$ as single systems and the number density is consistent with the UVLF at $M_{\text{UV}} \sim -20$ (Harikane et al. 2023b). At $z = 6 - 8$, we estimate the number density to be $(1 - 5) \times 10^{-5} \text{ cMpc}^{-3}$, and this value is enough to be observed by recent JWST surveys. The EIGER survey (Kashino et al. 2023) conducted deep JWST/NIRCam wide-field slitless spectroscopic observations and identified 117 [OIII] emitters at $z = 5.33 - 6.93$ (Matthee et al. 2023). They found that $\sim 1\%$ of their observed [OIII] emitters are closely separated within $< 1''$ (corresponding to $\lesssim 6 \text{ kpc}$ at $z \sim 6$). They also derived the [OIII] luminosity function at $z \sim 6$. We integrate it within the luminosity range for their samples and obtain the number density of their observed [OIII] emitters, $n_{[\text{OIII}]} = 10^{-2.8} \text{ cMpc}^{-3}$. Thus we can estimate the number density of clumpy systems of their observed [OIII] emitters as $\sim 0.01 \times n_{[\text{OIII}]} = 1.6 \times 10^{-5} \text{ cMpc}^{-3}$, consistent with our theoretical abundance of clumpy galaxies at $z = 6 - 8$.

We can also derive the merger rate density from the clumpy systems within a $10 \text{ kpc} \times 10 \text{ kpc}$ region following Mo et al. (2010). Under the assumption that these pairs will merge on a time scale τ_{mrg} , the merger rate density is related to the clumpy factor $f_{\text{clumpy}} \equiv (\# \text{ of clumpy systems with } N_{\text{clump}} \geq 2) / (\# \text{ of total systems})$,

⁷ We use the scaling relation between stellar mass and UV magnitude obtained from Ceverino et al. (2017, 2019) as follows,

$$M_{\text{UV}} = \frac{\log_{10} M_* - 6}{\alpha_*} + M_*^* \text{ (for } z = 6 - 7), \quad (11)$$

$$M_{\text{UV}} = \frac{\log_{10} M_* - 6}{\alpha_*} + M_*^* - 1 \text{ (for } z = 8 - 9), \quad (12)$$

where $\alpha_* = -0.394 \pm 0.002$ and $M_*^* = -12.13 \pm 0.03$.

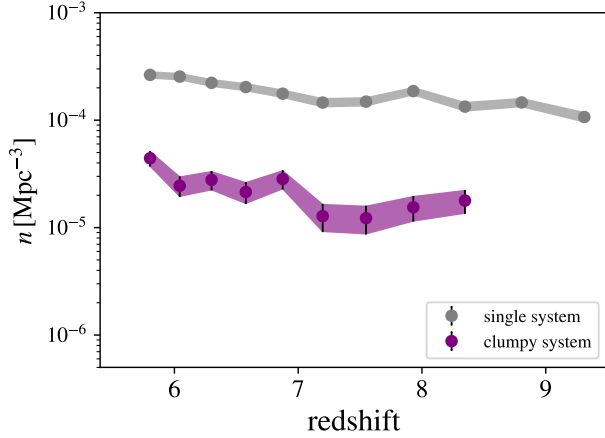


Figure 8. The number density of clumpy galaxies as a function of redshift. The gray and purple plots represent single systems and clumpy systems, respectively. The error bars are calculated from Poisson errors, \sqrt{N}/V_{box} , where N is the number of clumpy galaxies and V_{box} is the comoving volume of the simulation box.

according to

$$\begin{aligned} \dot{n}_{\text{mrg}} &= \frac{1}{\langle N_{\text{clump}} \rangle} \frac{f_{\text{clumpy}} n_{\text{gal}}}{\tau_{\text{mrg}}} \\ &= 6.3 \times 10^{-5} \text{ cMpc}^{-3} \text{ Gyr}^{-1} \\ &\times \left(\frac{f_{\text{clumpy}}}{0.1} \right) \left(\frac{n_{\text{gal}}}{10^{-4} \text{ cMpc}^{-3}} \right) \left(\frac{\tau_{\text{mrg}}}{80 \text{ Myr}} \right)^{-1}, \end{aligned} \quad (13)$$

where $\langle N_{\text{clump}} \rangle$ is the averaged clump number among clumpy systems. The factor $1/\langle N_{\text{clump}} \rangle$ takes into account the fact that a multi-clump system ends in a single merger. Figure 7 shows that $\sim 80 - 90\%$ of clumpy systems consist of two clumps, and we thus adopt $\langle N_{\text{clump}} \rangle = 2$. We obtain the clumpy factor from Figure 8 as $f_{\text{clumpy}} \sim 0.1 - 0.2$ and see that the value does not change very much at $z = 6 - 9$. For the comoving number density of galaxies population n_{gal} , we obtain $n_{\text{gal}} \sim 10^{-4} \text{ cMpc}^{-3}$ with $M_* \gtrsim 10^9 M_{\odot}$ ⁸ from Figure 8. The value also does not change largely within a factor of 1-2. We adopt the crossing timescale (eq. (10)) as the merger timescale τ_{mrg} . In our case, we take into account a galaxy pair located within a $10 \text{ kpc} \times 10 \text{ kpc}$ region, i.e., the separation of $d \sim 5 \text{ kpc}$, which gives $\tau_{\text{mrg}} \sim 80 \text{ Myr}$. The merge timescale is also seen in the top panels of Figure 5. Adopting this merger as a typical case, the merger rate density is $\dot{n}_{\text{mrg}} = 6.3 \times 10^{-5} \text{ cMpc}^{-3} \text{ Gyr}^{-1}$. This value is roughly

consistent with the results from Millennium Simulation at $z > 6$ (fig.2 in Kitzbichler & White 2008). We also compare our merger rate density with that of Illustris simulations. Rodriguez-Gomez et al. (2015) derive the major merger rate $\sim 1 \text{ Gyr}^{-1}$ for the descendant stellar masses of $\sim 10^9 M_{\odot}$ at $z = 6 - 9$. From the stellar mass function at $z > 6$ of Illustris simulations (Genel et al. 2014), the corresponding number density of the descendant mass is $\sim 10^{-4} \text{ cMpc}^{-3}$. Therefore, the major merger rate density is $\sim 10^{-4} \text{ cMpc}^{-3} \text{ Gyr}^{-1}$, which is in good agreement with our values. These consistencies infer that clumpy galaxies, which are bright in rest-frame optical emission lines, can be linked to major mergers.

4. DISCUSSION & SUMMARY

We have studied formation of clumpy galaxies in the epoch of reionization observable in rest-frame optical emission lines. The clumps we identify are bright in [OIII] 5007Å and have radii of $\sim 150 - 200 \text{ pc}$, which can be resolved by JWST. We have shown that the observable large clumps are formed by major mergers. The clumps are categorized into two types: proto-bulges dominated by stellar populations older than 50 Myr and off-centered clumps dominated by younger stellar populations. The latter type of clump is formed from gas debris in tidal tails induced by the mergers. The merger-driven clumps tend to have a high gas fraction of over 90%, trigger bursty star formation with sSFR $\sim 20 - 100 \text{ Gyr}^{-1}$, and produce young stellar components. The clumpy galaxies account for $\sim 10\%$ of the population, and the fraction remains roughly constant from $z = 9$ to $z = 6$. We also find that the clumpy systems are short-lived, ending in a merger with companion(s) within a few tens of Myrs. The number density of clumpy systems is estimated to be $(1-5) \times 10^{-5} \text{ cMpc}^{-3}$, which is large enough to be observed in recent JWST surveys (Matthee et al. 2023).

Formation of clumpy galaxies at $z \lesssim 4$ has been studied in detail (Mandelker et al. 2014, 2017; Buck et al. 2017; Ceverino et al. 2023). Especially, Mandelker et al. (2014) study clump formation in 29 galaxy samples at $z = 1 - 4$. They define clumps as baryonic overdensities in three dimensions. They find that 70% of the clumps are formed *in situ* by violent disk instability while the remaining 30% are formed *ex situ* by minor mergers. In the present paper, we study clump formation at $z = 6 - 9$ using high-resolution simulations. We define the clumps as [OIII] bright objects based on the threshold surface star formation rate so that they can be observed by JWST with a reasonable exposure time. We find that most of the observable clumps are formed

⁸ This stellar mass is for a galaxy system within $10 \text{ kpc} \times 10 \text{ kpc}$, not each clump stellar mass.

by mergers of galaxies with roughly the same baryonic mass. A sufficiently large “perturber” comparable to the central object with size ~ 200 pc can generate gas wakes and overdensities to form large, bright clumps. Interestingly, violent disk instability (VDI) is less likely to occur in low-mass galaxies because the disk mass itself is small (Dekel et al. 2009). In the VDI case, even when it occurs, clumps contain only 1-2 % of the mass of the central object (Ceverino et al. 2010), rendering them too faint to be detected through current observations. Our result suggests a change of the mode of clump formation from the predominantly merger-driven scenario in the early universe to VDI at low redshifts at $z \lesssim 4 - 5$.

There are still some caveats in our study. Firstly, we define clumps by adopting a constant threshold of surface star formation rate density. The constant value is motivated to identify observable clumps, but at the same time, we might miss clumps in low-mass galaxies at $z \sim 9$. Such unidentified low-mass clumps might correspond to proto-globular clusters. Recent JWST photometric observations in gravitational lens fields have found young stellar cluster candidates with $M_* = 10^5 - 10^6 M_\odot$ at $z = 6 - 10$ (Vanzella et al. 2022, 2023; Adamo et al. 2024). The star clusters are also very small in size with effective radii of less than 1 pc, which even zoom-in simulations cannot resolve. Second, our clump identification is based on rest-frame emission lines. Statistics of high- z clumpy galaxies have been conducted from rest-frame UV observation by HST (e.g. Shibuya et al. 2016; Bowler et al. 2017, 2022), and recent JWST NIRCам and NIRSpec/MIRI IFU observations have revealed that the number of clumps is often different between UV and Near-IR (Bik et al. 2023; Kalita et al. 2024). Dust attenuation may cause a significant effect on the clump identification in the rest-frame UV because clumps are formed in dense clouds of $n_{\text{gas}} \geq 100 \text{ cm}^{-3}$ (Figure 2) where large optical depth and UV attenuation are expected especially in clump regions. Post-process radiative transfer calculations using, for example, SKIRT (Baes et al. 2011; Camps & Baes 2020), will be needed to obtain spatially-resolved dust attenuation in future studies.

We have found that a clumpy system contains different stellar/clump populations: old (> 50 Myr) clumps at the center of dark matter halos, and young (< 50 Myr) off-centered clumps. The latter type of clumps are formed in dense gas clouds formed in tidal tails during merg-

ers. Observationally, it would be interesting to identify old clumps with ages of a few hundred Myrs. As shown in Figure 2, there are spatial offsets between the young ($\lesssim 50$ Myr) and old (~ 300 Myr) components. Those old components are not detected as a clump based on our criteria. Recent JWST observations show that some clumps are detected in rest-frame optical emission lines and continuum, while others are detected only in continuum (e.g. Hashimoto et al. 2023). Detailed radiative transfer calculations would also enable us to understand the cause of the spatial offsets between young stellar populations and dust continuum emitting regions as seen in recent observations at $z = 8.3$ (Tamura et al. 2023).

Emission line flux ratios provide crucial information on clump properties such as the ISM electron density, metallicity, and ionization parameter. For instance, Yang et al. (2023) use a zoom-in simulation to show that the ratio of $F_{[\text{OIII}] 5007 \text{ \AA}}/F_{[\text{OII}] 3727 \text{ \AA}}$ can be used to trace stellar populations younger than several Myr. The ratio is taken by some NIRSpec IFU observations to evaluate the ionization state in each pixel (Arribas et al. 2023; Saxena et al. 2024). Line ratios are also measured for $z \sim 4$ lensed galaxies to determine and produce resolved metallicity and dust-to-gas ratio maps (Birkin et al. 2023). Applying the same method to clumpy galaxies at higher redshift will enable us to characterize young and old clumps and to test the merger-driven scenario we propose here.

ACKNOWLEDGEMENTS

We are grateful to thank Takatoshi Shibuya, Takuya Hashimoto, Yuma Sugahara, Javier Álvarez-Márquez, Luis Colina, Luca Constantin, Carmen Blanco Prieto for the fruitful discussion. This work made use of v2.3 of the Binary Population and Spectral Synthesis (BPASS) models as described in Byrne et al. (2022) and Stanway & Eldridge (2018). The authors thankfully acknowledge the computer resources at MareNostrum and the technical support provided by the Barcelona Supercomputing Center (RES-AECT-2020-3-0019). Numerical analyses were carried out on the analysis servers at Center for Computational Astrophysics, National Astronomical Observatory of Japan. YN acknowledges funding from JSPS KAKENHI Grant Number 23KJ0728 and a JSR fellowship. DC is a Ramon-Cajal Researcher and is supported by the Ministerio de Ciencia, Innovación y Universidades (MICIU/FEDER) under research grant PID2021-122603NB-C21.

APPENDIX

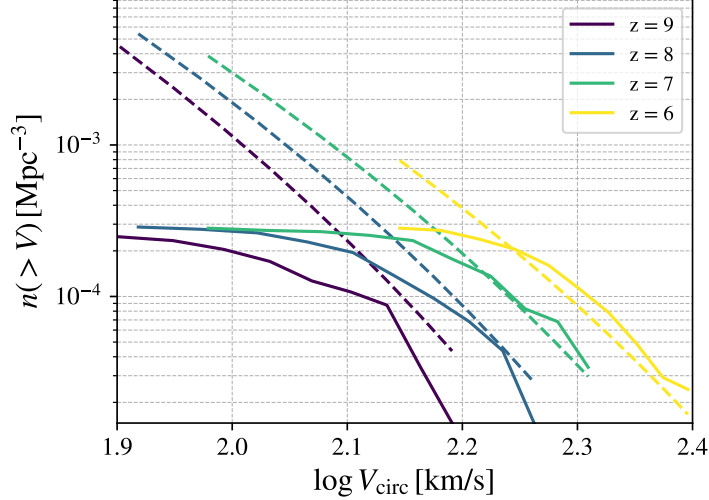


Figure 9. Velocity function of halos at $z=9$ (purple), 8(blue), 7(green), and 6(yellow). Solid lines are obtained from FirstLight 62 samples and dashed lines are from the Bolshoi simulation using the same cosmological parameter (Klypin et al. 2011).

A. ABUNDANCE MATCHING

FirstLight simulation provides a velocity selected sample of massive galaxies with $\log V_{\text{circ}} [\text{km/s}] \geq 2.3$ at $z = 5$. The output of the zoom-in simulations contains the galaxies and their progenitors, but not other smaller galaxies in a cosmological volume. In order to estimate the comoving number density of low mass galaxies, we use the circular velocity function of Bolshoi N -body simulation, which has a larger volume of $(250 h^{-1} \text{cMpc})^3$ (Klypin et al. 2011, 2016; Rodríguez-Puebla et al. 2016). Figure 9 compares the velocity functions at $z = 9 - 6$ obtained from FirstLight (solid lines) with those from the Bolshoi simulation (dashed lines). The latter can be well approximated by

$$n(> V) = AV^{-3} \exp \left(- \left[\frac{V}{V_0} \right]^\alpha \right), \quad (\text{A1})$$

where

$$A = 1.52 \times 10^4 \sigma_8^{-3/4}(z) (h^{-1} \text{Mpc/kms}^{-1})^{-3}, \quad (\text{A2})$$

$$\alpha = 1 + 2.15 \sigma_8^{4/3}(z), \quad (\text{A3})$$

$$V_0 = 3300 \frac{\sigma_8^2(z)}{1 + 2.5 \sigma_8^2(z)} \text{ kms}^{-1}, \quad (\text{A4})$$

as derived in Klypin et al. (2011).

We reconstruct the halo and galaxy abundances in the following manner. We configure 20 velocity bins logarithmically scaled. In each bin, we calculate the ratio of the number density of the Bolshoi and FirstLight simulations, $R_i = n(> V_{\text{circ}})_{\text{Bolshoi}} / n(> V_{\text{circ}})_{\text{FL}}$. For each snapshot subscripted i , we compute the circular velocity ($V_{\text{circ},i}$) of the galaxy, and count the total number of galaxies within a velocity bin. We then use the ratio R_i as a weighting factor to derive the “true” number of single (clumpy) systems at a given redshift as

$$N_{\text{single(clumpy)}}(z_{\text{bin}}) = \sum_i^{\text{\#snap}(z_{\text{bin}})} \Theta R_i, \quad (\text{A5})$$

where Θ is set to 1 when snapshot i is single (clumpy) system and otherwise 0. Here $\text{\#snap}(z_{\text{bin}})$ represents the number of snapshots in each redshift bin. Dividing the number by the volume of the FirstLight simulation, i.e., $(40 \text{ cMpc}/h)^3$, we obtain the number density of the single or clumpy systems at each redshift in Figure 8.

REFERENCES

- Adamo, A., Bradley, L. D., Vanzella, E., et al. 2024, arXiv e-prints, arXiv:2401.03224, doi: 10.48550/arXiv.2401.03224
- Agertz, O., Teyssier, R., & Moore, B. 2009, MNRAS, 397, L64, doi: 10.1111/j.1745-3933.2009.00685.x

- Álvarez-Márquez, J., Colina, L., Crespo Gómez, A., et al. 2023, arXiv e-prints, arXiv:2309.06319, doi: [10.48550/arXiv.2309.06319](https://doi.org/10.48550/arXiv.2309.06319)
- Arata, S., Yajima, H., Nagamine, K., Abe, M., & Khochfar, S. 2020, MNRAS, 498, 5541, doi: [10.1093/mnras/staa2809](https://doi.org/10.1093/mnras/staa2809)
- Arrabal Haro, P., Dickinson, M., Finkelstein, S. L., et al. 2023, arXiv e-prints, arXiv:2303.15431, doi: [10.48550/arXiv.2303.15431](https://doi.org/10.48550/arXiv.2303.15431)
- Arribas, S., Perna, M., Rodríguez Del Pino, B., et al. 2023, arXiv e-prints, arXiv:2312.00899, doi: [10.48550/arXiv.2312.00899](https://doi.org/10.48550/arXiv.2312.00899)
- Asada, Y., Sawicki, M., Abraham, R., et al. 2024, MNRAS, 527, 11372, doi: [10.1093/mnras/stad3902](https://doi.org/10.1093/mnras/stad3902)
- Baes, M., Verstaappen, J., De Looze, I., et al. 2011, ApJS, 196, 22, doi: [10.1088/0067-0049/196/2/22](https://doi.org/10.1088/0067-0049/196/2/22)
- Barrow, K. S. S., Wise, J. H., Norman, M. L., O’Shea, B. W., & Xu, H. 2017, MNRAS, 469, 4863, doi: [10.1093/mnras/stx1181](https://doi.org/10.1093/mnras/stx1181)
- Bertoldi, F., & McKee, C. F. 1992, ApJ, 395, 140, doi: [10.1086/171638](https://doi.org/10.1086/171638)
- Bik, A., Álvarez-Márquez, J., Colina, L., et al. 2023, arXiv e-prints, arXiv:2312.03074, doi: [10.48550/arXiv.2312.03074](https://doi.org/10.48550/arXiv.2312.03074)
- Birkin, J. E., Hutchison, T. A., Welch, B., et al. 2023, ApJ, 958, 64, doi: [10.3847/1538-4357/acf712](https://doi.org/10.3847/1538-4357/acf712)
- Bowler, R. A. A., Cullen, F., McLure, R. J., Dunlop, J. S., & Avison, A. 2022, MNRAS, 510, 5088, doi: [10.1093/mnras/stab3744](https://doi.org/10.1093/mnras/stab3744)
- Bowler, R. A. A., Dunlop, J. S., McLure, R. J., & McLeod, D. J. 2017, MNRAS, 466, 3612, doi: [10.1093/mnras/stw3296](https://doi.org/10.1093/mnras/stw3296)
- Bradač, M., Strait, V., Mowla, L., et al. 2023, arXiv e-prints, arXiv:2308.13288, doi: [10.48550/arXiv.2308.13288](https://doi.org/10.48550/arXiv.2308.13288)
- Buck, T., Macciò, A. V., Obreja, A., et al. 2017, MNRAS, 468, 3628, doi: [10.1093/mnras/stx685](https://doi.org/10.1093/mnras/stx685)
- Byrne, C. M., Stanway, E. R., Eldridge, J. J., McSwiney, L., & Townsend, O. T. 2022, MNRAS, 512, 5329, doi: [10.1093/mnras/stac807](https://doi.org/10.1093/mnras/stac807)
- Camps, P., & Baes, M. 2020, Astronomy and Computing, 31, 100381, doi: [10.1016/j.ascom.2020.100381](https://doi.org/10.1016/j.ascom.2020.100381)
- Ceverino, D., Dekel, A., & Bournaud, F. 2010, MNRAS, 404, 2151, doi: [10.1111/j.1365-2966.2010.16433.x](https://doi.org/10.1111/j.1365-2966.2010.16433.x)
- Ceverino, D., Glover, S. C. O., & Klessen, R. S. 2017, MNRAS, 470, 2791, doi: [10.1093/mnras/stx1386](https://doi.org/10.1093/mnras/stx1386)
- Ceverino, D., Klessen, R. S., & Glover, S. C. O. 2019, MNRAS, 484, 1366, doi: [10.1093/mnras/stz079](https://doi.org/10.1093/mnras/stz079)
- Ceverino, D., & Klypin, A. 2009, ApJ, 695, 292, doi: [10.1088/0004-637X/695/1/292](https://doi.org/10.1088/0004-637X/695/1/292)
- Ceverino, D., Klypin, A., Klimek, E. S., et al. 2014, MNRAS, 442, 1545, doi: [10.1093/mnras/stu956](https://doi.org/10.1093/mnras/stu956)
- Ceverino, D., Mandelker, N., Snyder, G. F., et al. 2023, MNRAS, 522, 3912, doi: [10.1093/mnras/stad1255](https://doi.org/10.1093/mnras/stad1255)
- Ceverino, D., Primack, J., & Dekel, A. 2015, MNRAS, 453, 408, doi: [10.1093/mnras/stv1603](https://doi.org/10.1093/mnras/stv1603)
- Chen, Z., Stark, D. P., Endsley, R., et al. 2023, MNRAS, 518, 5607, doi: [10.1093/mnras/stac3476](https://doi.org/10.1093/mnras/stac3476)
- Colina, L., Crespo Gómez, A., Álvarez-Márquez, J., et al. 2023, A&A, 673, L6, doi: [10.1051/0004-6361/202346535](https://doi.org/10.1051/0004-6361/202346535)
- Curtis-Lake, E., Carniani, S., Cameron, A., et al. 2023, Nature Astronomy, 7, 622, doi: [10.1038/s41550-023-01918-w](https://doi.org/10.1038/s41550-023-01918-w)
- Dekel, A., & Krumholz, M. R. 2013, MNRAS, 432, 455, doi: [10.1093/mnras/stt480](https://doi.org/10.1093/mnras/stt480)
- Dekel, A., Sari, R., & Ceverino, D. 2009, ApJ, 703, 785, doi: [10.1088/0004-637X/703/1/785](https://doi.org/10.1088/0004-637X/703/1/785)
- Di Matteo, P., Bournaud, F., Martig, M., et al. 2008, A&A, 492, 31, doi: [10.1051/0004-6361:200809480](https://doi.org/10.1051/0004-6361:200809480)
- Eldridge, J. J., Stanway, E. R., Xiao, L., et al. 2017, PASA, 34, e058, doi: [10.1017/pasa.2017.51](https://doi.org/10.1017/pasa.2017.51)
- Ferland, G. J., Porter, R. L., van Hoof, P. A. M., et al. 2013, RMxAA, 49, 137. <https://arxiv.org/abs/1302.4485>
- Fujimoto, S., Ouchi, M., Nakajima, K., et al. 2022, arXiv e-prints, arXiv:2212.06863, doi: [10.48550/arXiv.2212.06863](https://doi.org/10.48550/arXiv.2212.06863)
- Gelli, V., Salvadori, S., Ferrara, A., Pallottini, A., & Carniani, S. 2021, ApJL, 913, L25, doi: [10.3847/2041-8213/abfe6c](https://doi.org/10.3847/2041-8213/abfe6c)
- Gelli, V., Salvadori, S., Pallottini, A., & Ferrara, A. 2020, MNRAS, 498, 4134, doi: [10.1093/mnras/staa2410](https://doi.org/10.1093/mnras/staa2410)
- Genel, S., Vogelsberger, M., Springel, V., et al. 2014, MNRAS, 445, 175, doi: [10.1093/mnras/stu1654](https://doi.org/10.1093/mnras/stu1654)
- Guo, Y., Ferguson, H. C., Bell, E. F., et al. 2015, ApJ, 800, 39, doi: [10.1088/0004-637X/800/1/39](https://doi.org/10.1088/0004-637X/800/1/39)
- Hainline, K. N., Johnson, B. D., Robertson, B., et al. 2023, arXiv e-prints, arXiv:2306.02468, doi: [10.48550/arXiv.2306.02468](https://doi.org/10.48550/arXiv.2306.02468)
- Harikane, Y., Nakajima, K., Ouchi, M., et al. 2023a, arXiv e-prints, arXiv:2304.06658, doi: [10.48550/arXiv.2304.06658](https://doi.org/10.48550/arXiv.2304.06658)
- Harikane, Y., Ouchi, M., Inoue, A. K., et al. 2020, ApJ, 896, 93, doi: [10.3847/1538-4357/ab94bd](https://doi.org/10.3847/1538-4357/ab94bd)
- Harikane, Y., Ouchi, M., Oguri, M., et al. 2023b, ApJS, 265, 5, doi: [10.3847/1538-4365/acaaa9](https://doi.org/10.3847/1538-4365/acaaa9)
- Hashimoto, T., Laporte, N., Mawatari, K., et al. 2018, Nature, 557, 392, doi: [10.1038/s41586-018-0117-z](https://doi.org/10.1038/s41586-018-0117-z)
- Hashimoto, T., Álvarez-Márquez, J., Fudamoto, Y., et al. 2023, ApJL, 955, L2, doi: [10.3847/2041-8213/acf57c](https://doi.org/10.3847/2041-8213/acf57c)

- Hirschmann, M., Charlot, S., Feltre, A., et al. 2017, *MNRAS*, 472, 2468, doi: [10.1093/mnras/stx2180](https://doi.org/10.1093/mnras/stx2180)
- . 2022, arXiv e-prints, arXiv:2212.02522, <https://arxiv.org/abs/2212.02522>
- Hopkins, P. F., Croton, D., Bundy, K., et al. 2010, *ApJ*, 724, 915, doi: [10.1088/0004-637X/724/2/915](https://doi.org/10.1088/0004-637X/724/2/915)
- Hsiao, T. Y.-Y., Coe, D., Abdurro'uf, et al. 2023a, *ApJL*, 949, L34, doi: [10.3847/2041-8213/acc94b](https://doi.org/10.3847/2041-8213/acc94b)
- Hsiao, T. Y.-Y., Abdurro'uf, Coe, D., et al. 2023b, arXiv e-prints, arXiv:2305.03042, doi: [10.48550/arXiv.2305.03042](https://doi.org/10.48550/arXiv.2305.03042)
- Isobe, Y., Ouchi, M., Nakajima, K., et al. 2023, arXiv e-prints, arXiv:2301.06811, doi: [10.48550/arXiv.2301.06811](https://doi.org/10.48550/arXiv.2301.06811)
- Jones, G. C., Ubler, H., Perna, M., et al. 2023, arXiv e-prints, arXiv:2308.16620, doi: [10.48550/arXiv.2308.16620](https://doi.org/10.48550/arXiv.2308.16620)
- Kalita, B. S., Silverman, J. D., Daddi, E., et al. 2024, arXiv e-prints, arXiv:2402.02679, doi: [10.48550/arXiv.2402.02679](https://doi.org/10.48550/arXiv.2402.02679)
- Kashino, D., Lilly, S. J., Matthee, J., et al. 2023, *ApJ*, 950, 66, doi: [10.3847/1538-4357/acc588](https://doi.org/10.3847/1538-4357/acc588)
- Katz, H., Galligan, T. P., Kimm, T., et al. 2019, *MNRAS*, 487, 5902, doi: [10.1093/mnras/stz1672](https://doi.org/10.1093/mnras/stz1672)
- Kitzbichler, M. G., & White, S. D. M. 2008, *MNRAS*, 391, 1489, doi: [10.1111/j.1365-2966.2008.13873.x](https://doi.org/10.1111/j.1365-2966.2008.13873.x)
- Klypin, A., Yepes, G., Gottlöber, S., Prada, F., & Heß, S. 2016, *MNRAS*, 457, 4340, doi: [10.1093/mnras/stw248](https://doi.org/10.1093/mnras/stw248)
- Klypin, A. A., Trujillo-Gomez, S., & Primack, J. 2011, *ApJ*, 740, 102, doi: [10.1088/0004-637X/740/2/102](https://doi.org/10.1088/0004-637X/740/2/102)
- Kravtsov, A. V. 2003, *ApJL*, 590, L1, doi: [10.1086/376674](https://doi.org/10.1086/376674)
- Kravtsov, A. V., Klypin, A. A., & Khokhlov, A. M. 1997, *ApJS*, 111, 73, doi: [10.1086/313015](https://doi.org/10.1086/313015)
- Ma, X., Hopkins, P. F., Garrison-Kimmel, S., et al. 2018, *MNRAS*, 478, 1694, doi: [10.1093/mnras/sty1024](https://doi.org/10.1093/mnras/sty1024)
- Mandelker, N., Dekel, A., Ceverino, D., et al. 2017, *MNRAS*, 464, 635, doi: [10.1093/mnras/stw2358](https://doi.org/10.1093/mnras/stw2358)
- . 2014, *MNRAS*, 443, 3675, doi: [10.1093/mnras/stu1340](https://doi.org/10.1093/mnras/stu1340)
- Matthee, J., Mackenzie, R., Simcoe, R. A., et al. 2023, *ApJ*, 950, 67, doi: [10.3847/1538-4357/acc846](https://doi.org/10.3847/1538-4357/acc846)
- Mo, H., van den Bosch, F. C., & White, S. 2010, *Galaxy Formation and Evolution*
- Mushtaq, M., Ceverino, D., Klessen, R. S., Reissl, S., & Puttasiddappa, P. H. 2023, *MNRAS*, 525, 4976, doi: [10.1093/mnras/stad2602](https://doi.org/10.1093/mnras/stad2602)
- Nakazato, Y., Yoshida, N., & Ceverino, D. 2023, *ApJ*, 953, 140, doi: [10.3847/1538-4357/ace25a](https://doi.org/10.3847/1538-4357/ace25a)
- Osterbrock, D. E., & Ferland, G. J. 2006, *Astrophysics of gaseous nebulae and active galactic nuclei*
- Pillepich, A., Springel, V., Nelson, D., et al. 2018, *MNRAS*, 473, 4077, doi: [10.1093/mnras/stx2656](https://doi.org/10.1093/mnras/stx2656)
- Planck Collaboration, Ade, P. A. R., Aghanim, N., et al. 2014, *A&A*, 571, A16, doi: [10.1051/0004-6361/201321591](https://doi.org/10.1051/0004-6361/201321591)
- Popesso, P., Concas, A., Cresci, G., et al. 2023, *MNRAS*, 519, 1526, doi: [10.1093/mnras/stac3214](https://doi.org/10.1093/mnras/stac3214)
- Renaud, F., Bournaud, F., & Duc, P.-A. 2015, *MNRAS*, 446, 2038, doi: [10.1093/mnras/stu2208](https://doi.org/10.1093/mnras/stu2208)
- Renaud, F., Bournaud, F., Kraljic, K., & Duc, P. A. 2014, *MNRAS*, 442, L33, doi: [10.1093/mnrasl/slu050](https://doi.org/10.1093/mnrasl/slu050)
- Renaud, F., Bournaud, F., Emsellem, E., et al. 2013, *MNRAS*, 436, 1836, doi: [10.1093/mnras/stt1698](https://doi.org/10.1093/mnras/stt1698)
- Ribeiro, B., Le Fèvre, O., Cassata, P., et al. 2017, *A&A*, 608, A16, doi: [10.1051/0004-6361/201630057](https://doi.org/10.1051/0004-6361/201630057)
- Rodriguez-Gomez, V., Genel, S., Vogelsberger, M., et al. 2015, *MNRAS*, 449, 49, doi: [10.1093/mnras/stv264](https://doi.org/10.1093/mnras/stv264)
- Rodriguez-Gomez, V., Pillepich, A., Sales, L. V., et al. 2016, *MNRAS*, 458, 2371, doi: [10.1093/mnras/stw456](https://doi.org/10.1093/mnras/stw456)
- Rodríguez-Puebla, A., Behroozi, P., Primack, J., et al. 2016, *MNRAS*, 462, 893, doi: [10.1093/mnras/stw1705](https://doi.org/10.1093/mnras/stw1705)
- Romano, M., Cassata, P., Morselli, L., et al. 2021, *A&A*, 653, A111, doi: [10.1051/0004-6361/202141306](https://doi.org/10.1051/0004-6361/202141306)
- Saxena, A., Overzier, R. A., Villar-Martín, M., et al. 2024, arXiv e-prints, arXiv:2401.12199, doi: [10.48550/arXiv.2401.12199](https://doi.org/10.48550/arXiv.2401.12199)
- Shibuya, T., Miura, N., Iwate, K., et al. 2022, *PASJ*, 74, 73, doi: [10.1093/pasj/psab111](https://doi.org/10.1093/pasj/psab111)
- Shibuya, T., Ouchi, M., Kubo, M., & Harikane, Y. 2016, *ApJ*, 821, 72, doi: [10.3847/0004-637X/821/2/72](https://doi.org/10.3847/0004-637X/821/2/72)
- Shimizu, I., Inoue, A. K., Okamoto, T., & Yoshida, N. 2014, *MNRAS*, 440, 731, doi: [10.1093/mnras/stu265](https://doi.org/10.1093/mnras/stu265)
- Stanway, E. R., & Eldridge, J. J. 2018, *MNRAS*, 479, 75, doi: [10.1093/mnras/sty1353](https://doi.org/10.1093/mnras/sty1353)
- Tamura, Y., Mawatari, K., Hashimoto, T., et al. 2019, *ApJ*, 874, 27, doi: [10.3847/1538-4357/ab0374](https://doi.org/10.3847/1538-4357/ab0374)
- Tamura, Y., C. Bakx, T. J. L., Inoue, A. K., et al. 2023, *ApJ*, 952, 9, doi: [10.3847/1538-4357/acd637](https://doi.org/10.3847/1538-4357/acd637)
- Toomre, A. 1964, *ApJ*, 139, 1217, doi: [10.1086/147861](https://doi.org/10.1086/147861)
- Vanzella, E., Castellano, M., Bergamini, P., et al. 2022, *ApJL*, 940, L53, doi: [10.3847/2041-8213/ac8c2d](https://doi.org/10.3847/2041-8213/ac8c2d)
- Vanzella, E., Claeysens, A., Welch, B., et al. 2023, *ApJ*, 945, 53, doi: [10.3847/1538-4357/acb59a](https://doi.org/10.3847/1538-4357/acb59a)
- Wang, B., Fujimoto, S., Labbe, I., et al. 2023, arXiv e-prints, arXiv:2308.03745, doi: [10.48550/arXiv.2308.03745](https://doi.org/10.48550/arXiv.2308.03745)
- Yang, S., Lidz, A., Smith, A., Benson, A., & Li, H. 2023, *MNRAS*, 525, 5989, doi: [10.1093/mnras/stad2571](https://doi.org/10.1093/mnras/stad2571)